Supporting Information

Highly Active and Stable Iridium Pyrochlores for Oxygen Evolution Reaction

Dmitry Lebedev,[†] Mauro Povia,[‡] Kay Waltar,[‡,◊] Paula M. Abdala,[§] Ivano E. Castelli,[‖] Emiliana Fabbri,[‡] Maria V. Blanco,[⊥] Alexey Fedorov,[†,§] Christophe Copéret,[*,†] Nicola Marzari,[*,‖] and Thomas J. Schmidt[*,‡,†]

[†]ETH Zürich, Department of Chemistry and Applied Biosciences, Vladimir-Prelog-Weg 1-5, CH-8093 Zürich, Switzerland;

[‡]Electrochemistry Laboratory, Paul Scherrer Institute, CH-5232, Villigen PSI, Switzerland;

[§] Department of Mechanical and Process Engineering, ETH Zürich, Leonhardstrasse 21, CH-8092, Zürich, Switzerland;

[‖]Theory and Simulation of Materials (THEOS), and National Centre for Computational Design and Discovery of Novel Materials (MARVEL), EPFL, CH-1015 Lausanne, Switzerland;

[⊥]European Synchrotron Radiation Facility, BP 220, F-38043 Grenoble Cedex, France.

Present address:

[◊]Surface Physics Laboratory, Department of Physics, University of Zürich, Winterthurerstrasse 190, CH-8057 Zürich, Switzerland

*E-mail: ccoperet@ethz.ch

*E-mail: nicola.marzari@epfl.ch

*E-mail: thomasjustus.schmidt@psi.ch

Supporting Information for Lebedev, Povia, Waltar, Abdala, Castelli, Fabbri, Blanco, Fedorov, Copéret, Marzari, and Schmidt

Table of Contents

CHARACTERIZATION DATA

Experimental Procedures

Iridium pyrochlores were prepared utilizing the Adams fusion protocol recently reported by us for the synthesis of high surface area Ir oxides.[1] Herein we show that addition of the second metal in the reaction mixture allows for the formation of the pyrochlore structure.

General procedure

$IrCl_3 \cdot xH_2O$ (0.6 mmol) was mixed with metal nitrate (0.6-0.72 mmol) and excess of sodium nitrate (ca. 10 g). The obtained mixture was heated in an open crucible in a muffle furnace for 1-2h at 500 − 575 °C, cooled to room temperature, and the residue extensively washed with water and dried at 150 °C overnight under ca. 2 mbar to yield the pyrochlore material as a black powder (ca. 150-200 mg).

The synthesis conditions (metal ratios, heating temperature, and time) for each catalyst were optimized independently to prepare phase-pure materials. Based on the powder XRD data, formation of the iridium pyrochlores occurs at temperatures ≥ 500 °C likely from the preformed iridium oxide due to the easy decomposition of iridium chloride in molten sodium nitrate. The latter process occurs starting from 350 °C,[1] as exemplified on the Y−Ir pyrochlore (Figure S1). In all the cases, increase of the synthesis temperature (up to 550 or 575 °C) and time allowed for the formation of the targeted pyrochlore material. The optimal temperature for the synthesis of pyrochlores appears to correlate with the decomposition temperature of the *A* metal nitrate.

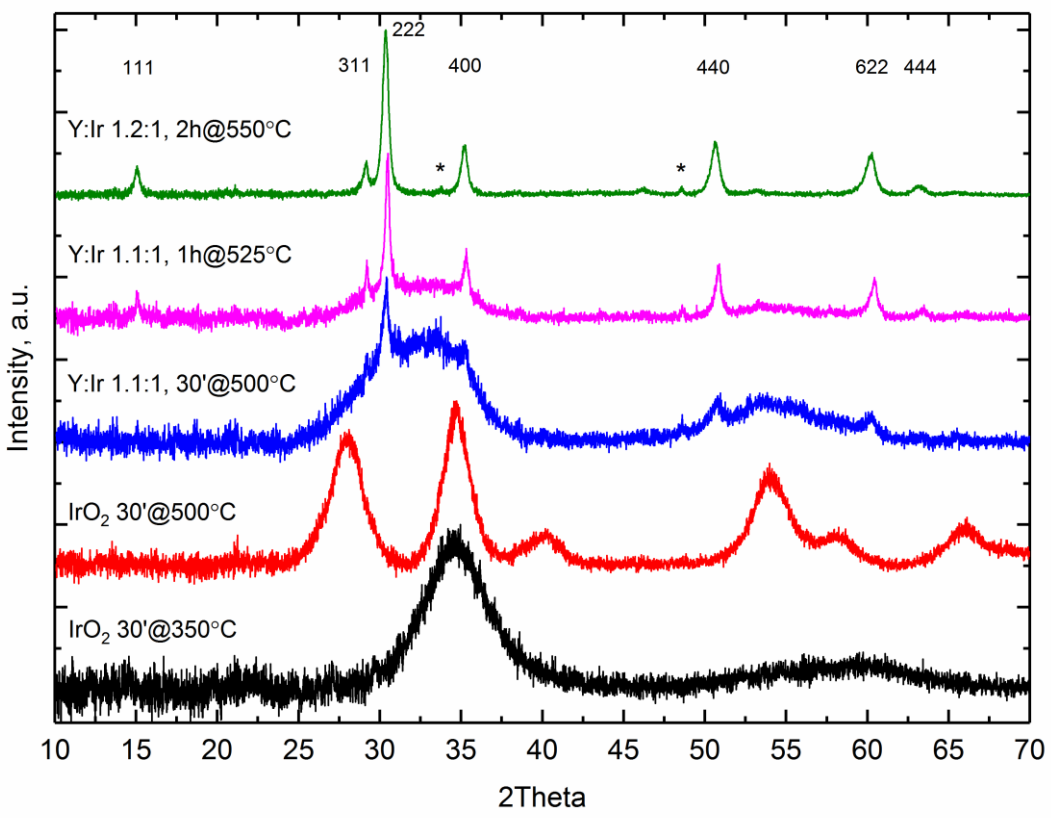

Figure S1. Powder XRD patterns of the iridium oxides and yttrium iridium pyrochlores prepared via Adams fusion method at different temperatures and reaction times. Miller indexes are shown for the pyrochlore peaks. (*) denotes Y_2O_3 impurity (peaks at 33.69 and 48.55 ° 2Theta); broad peaks present for yttrium iridium pyrochlores synthesized at 500 and 525 °C correspond to the iridium oxide phase (sample holder background was subtracted).

Synthesis of IrO_2 500 °C Adams (reference for XAS)

$IrCl_3 \cdot xH_2O$ (0.212 g, 0.6 mmol) and $NaNO_3$ (10 g) were dissolved in 100 mL of deionized H_2O, stirred for 10 min with sonication, and then dried under ca. 15 mbar to give a black powder. The powder was transferred into a porcelain crucible and heated in a muffle furnace at 500 °C for 5 h (heating program: 2°C min^{-1} to 150 °C, 30 min at 150 °C, ramp to 500 °C for 2 h). Thus-obtained sample was washed with deionized water and dried at 150 °C overnight under ca. 2 mbar to give IrO_2 as a black powder

Rietveld refinement and pair distribution function data analysis

Synchrotron X-ray total scattering measurements were performed at ID31 beamline at the European Synchrotron Radiation Facility (ESRF), Grenoble, France. Data were collected using wavelength of 0.15609 Å with a Pilatus CdTe 2M detector. The azimuthal integration was performed with pyFAI software[2] using CeO_2 powder as a standard. The sample was packed in a 1 mm Kapton capillary tube, data for two distinct sample-to-detector distances were collected. Rietveld refinement was carried out using the FullProf program,[3] over a Q range of 0.7–9 $Å^{-1}$ with the use of isotropic atomic displacement factors (Table S1). The use of anisotropic atomic displacement factors for Y and Ir did not improve the fit.

The pair distribution function (PDF, G(r)) was extracted using PDFgetx3[4] up to maximum Q of 23 $Å^{-1}$. Refinements of the PDF data were performed with PDFgui software. The PDF of the CeO_2 standard was used to determine the instrumental parameters (damping and broadening of PDF peaks due to experimental resolution), which were then fixed during the PDF refinements. The same model as for Rietveld refinement was used for the fitting of PDF data. Figure S3 displays the G(r) at short r-region and figure S4 shows the full G(r) up to 25 Å. The peak positions show good agreement with the interatomic distances obtained from Rietveld refinement of the pyrochlore structure. Y-Y, Ir-Ir (and Y-Ir) correlations contribute to the peak at 3.57 Å with no splitting observed in a good agreement with EXAFS results (Table S2). The fitting using the average structure model is shown in figure S4 (5.7% of Y_2O_3 phase was also included in the fitting), showing that the local structure is well explained by the average structure.

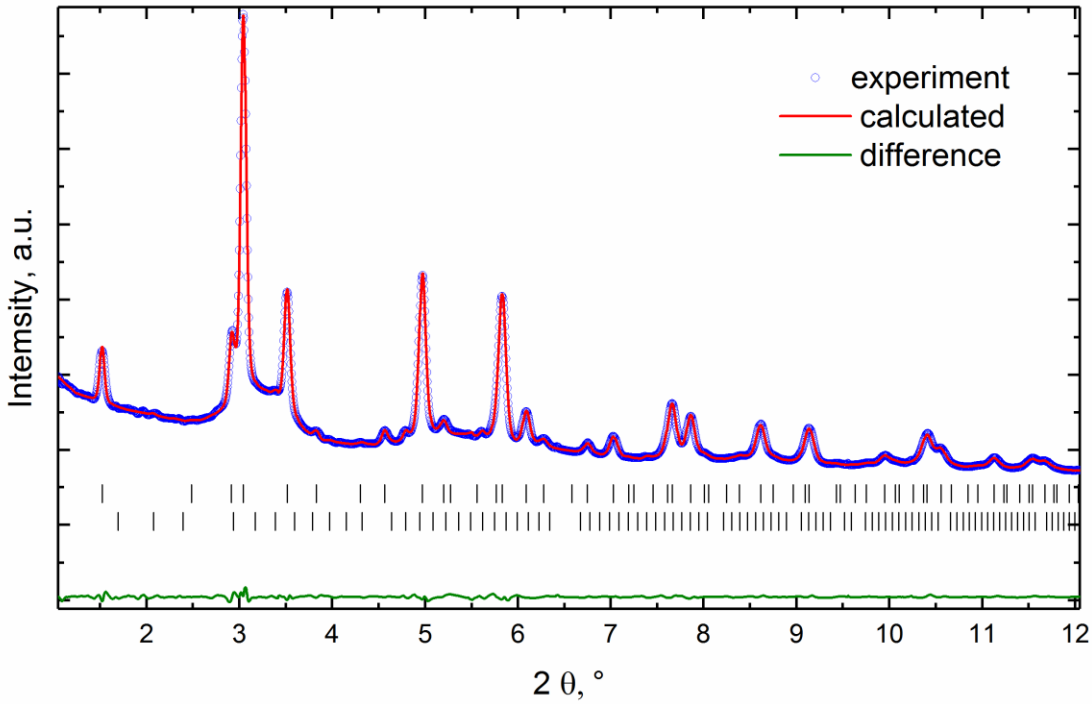

Figure S2. Powder XRD pattern of yttrium iridium pyrochlore measured at ESRF with 0.15609 Å radiation. The top set of reflection bars corresponds to pyrochlore phase, bottom − ca. 5.7% of Y_2O_3 impurity.

Table S1. Summary of structural parameters determined by Rietveld refinements of Y−Ir sample. Parameters given in bold were allowed to vary during the fitting.

Space group	$Fd\bar{3}m$				
a (Å)	**10.183(3)**				
	Atom parameters				
	x	*y*	*z*	U_{iso}, Å^2	*Occupancy*
Y (16e)	0.5	0.5	0.5	**0.0041(8)**	1.00
Ir (16c)	0	0	0	**0.0090(8)**	**0.915(1)**
Y (16c)	0	0	0	**0.0090(8)**	**0.084(1)**
O1 (48f)	0.125	0.125	0.125	**0.05(1)**	1.00
O2 (16e)	**0.3596(1)**	0.375	0.375	**0.05(1)**	1.00
Y_2O_3 content wt. %	**5.7 (2)**				
R_w	5.12				
R_{wp}	4.27				
R_{exp}	1.23				
χ^2	12.0				

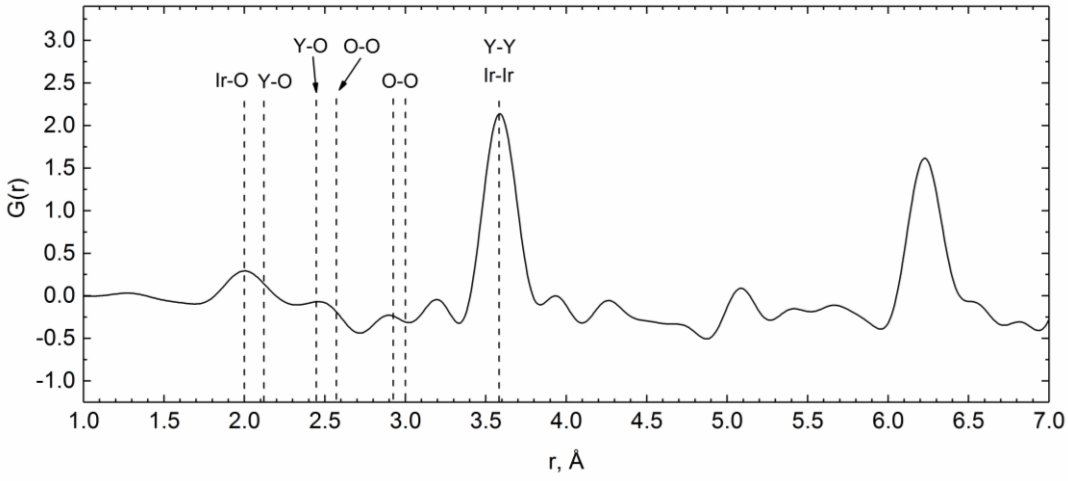

Figure S3. Short range of G(r) with element-element distances from $Y_2Ir_2O_7$ crystal structure

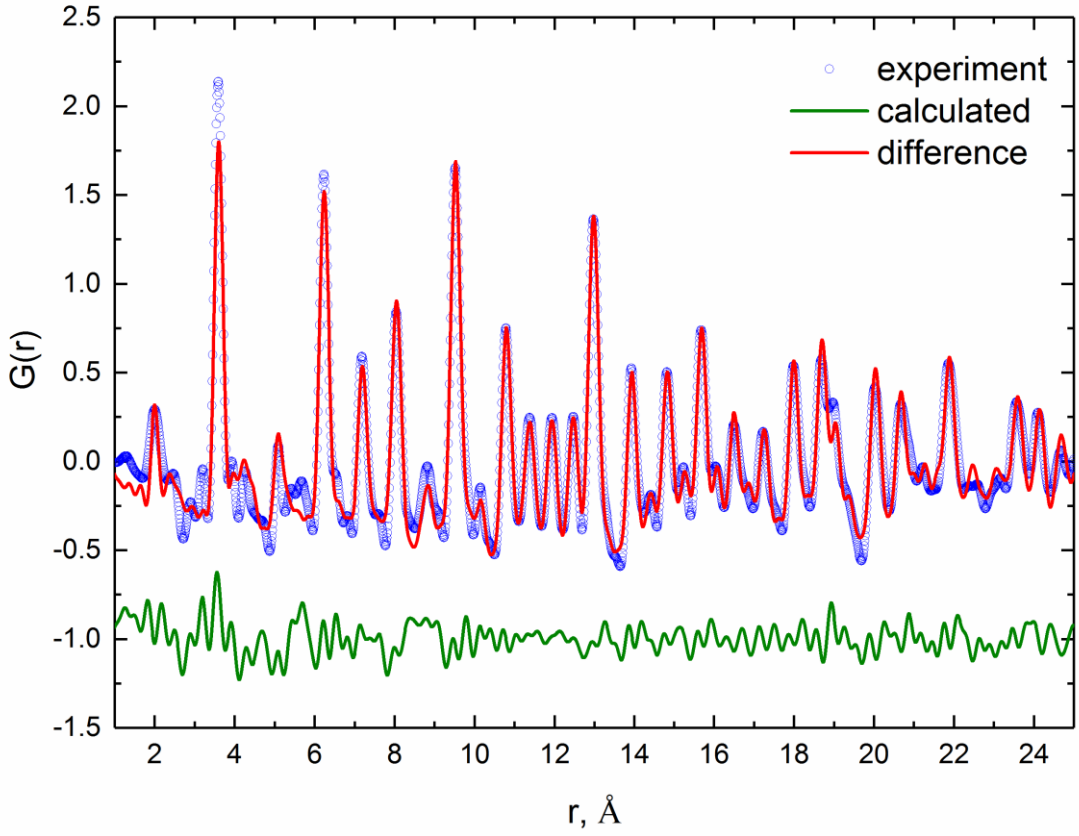

Figure S4. G(r) function fitted in the range 1-25 Å using the same model as for Rietveld refinement. *a* = 10.17(5) Å, R_w = 20%.

High resolution TEM images

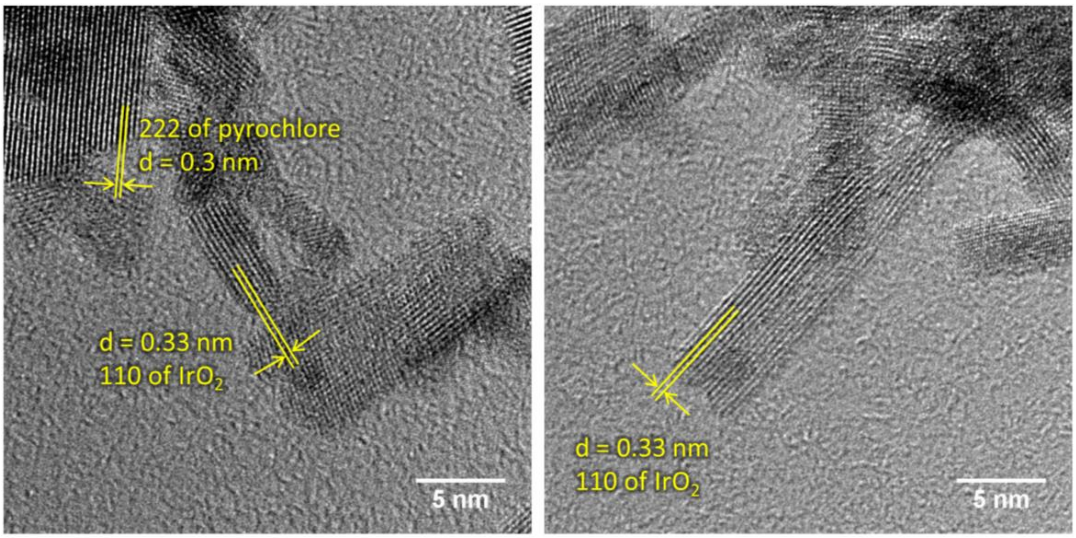

Figure S5. High resolution TEM (HRTEM) images of Pb−Ir pyrochlore, highlighting the presence of rod-shape nanoparticles of IrO_2 with 110 interplanar distance of 0.33 nm.

X-ray absorption (XAS) data

X−ray absorption (XAS) spectra were collected at the SuperXAS beamline of the Swiss Light Source (SLS) (PSI, Villigen, Switzerland). The SLS operates under top up mode at 2.4 GeV electron energy and a current of 400 mA. The incident beam was collimated by a Ru−coated mirror at 2.8 mrad and monochromatized using a channel−cut Si (111) monochromator. The beam with intensity of ~10^{12} ph s^{-1} was focused with a Rh coated toroidal mirror (at 2.8 mrad) down to 100 × 100 μm at the sample position. The beamline energy was calibrated with Pt reference foil to the Pt L_{III}−edge position at 11564 eV. Ionization chambers filled with N_2−Ar gas mixtures were used for XAS detection in transmission mode, where a Pt reference foil was measured congruently with the sample between the second and third ionization chambers.

The SuperXAS beamline[5] allowed for the rapid collection of >1000 spectra during a measurement time of ca. 10 min, which were then averaged. X−ray absorption data were analyzed using the Demeter program package,[6-7] which included energy calibration (based on the simultaneously measured Pt reference foil) background subtraction, and edge step normalization. To obtain Extended X−ray Absorption Fine Structure (EXAFS) data the resulting spectra were converted to the photoelectron wave vector *k* (in units $Å^{-1}$) by assigning the photoelectron energy origin, E_0, corresponding to k = 0, to the first inflection point. The resulting χ(*k*) functions were Fourier transformed over 3−12 $Å^{-1}$ for Bi−Ir and Pb−Ir and over 3−14 $Å^{-1}$ for Y−Ir, BiY−Ir, BiPb−Ir and YPb−Ir.

XANES spectra

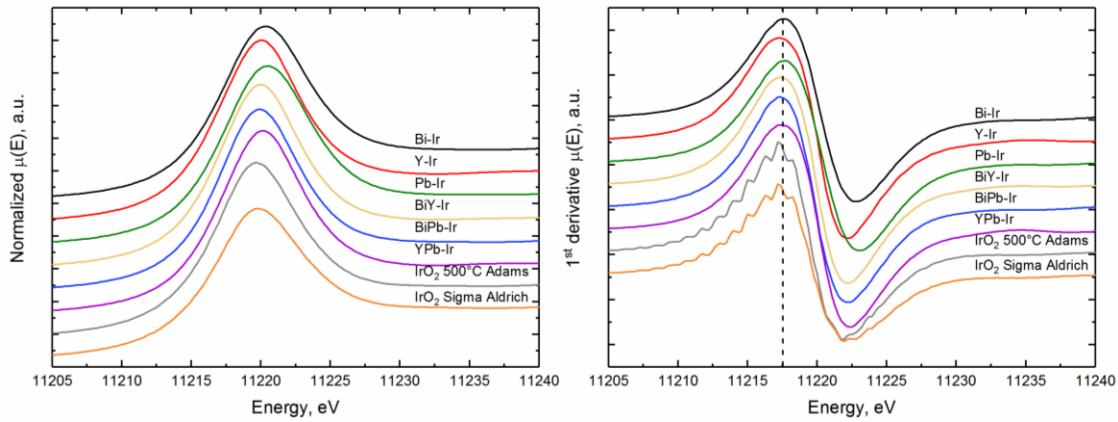

Figure S6. XANES and 1st derivative XANES spectra of pyrochlore materials and IrO_2 measured at L_{III} edge. IrO_2 was prepared at 500°C using same Adams fusion method (see above) and commercial IrO_2 was obtained from Sigma Aldrich

Analysis of EXAFS data

Extended X−ray absorption fine structure (EXAFS) data were analyzed using the Demeter program package. The theoretical model used for the EXAFS fitting was generated from $Bi_2Ir_2O_7$ and $Y_2Ir_2O_7$ pyrochlore structures using the FEFF6.2 library. Scattering paths for Pb−Ir, BiPb−Ir, and YPb−Ir pyrochlores were calculated based on the non-oxygen deficient $Bi_2Ir_2O_7$ pyrochlore structure, since there was found no evidence of the unsymmetrical Ir environment, present in the $Pb_2Ir_2O_{6.5}$ structure. Modeling of Pb−Ir, BiPb−Ir, and YPb−Ir using the paths generated from $Pb_2Ir_2O_{6.5}$ structure did not converge to reasonable fits. In order to capture the mixed occupancy of *A* position, BiY−Ir and YPb−Ir pyrochlores were modeled

using two paths for Bi/Pb and Y at ~3.6 Å (each with coordination number 3). The amplitude reduction factor, S_0^2, energy shift ΔE_0, Debye–Waller factor σ^2 and path length R were allowed to vary. Distance to the scattering center was modeled using the symmetrical expansion approach: $R = R_{eff} \cdot (delr + 1)$, where R_{eff} is distance calculated based on the crystal structure and *delr* was allowed to vary. The fitting was performed simultaneously in *k* weights 1-3.

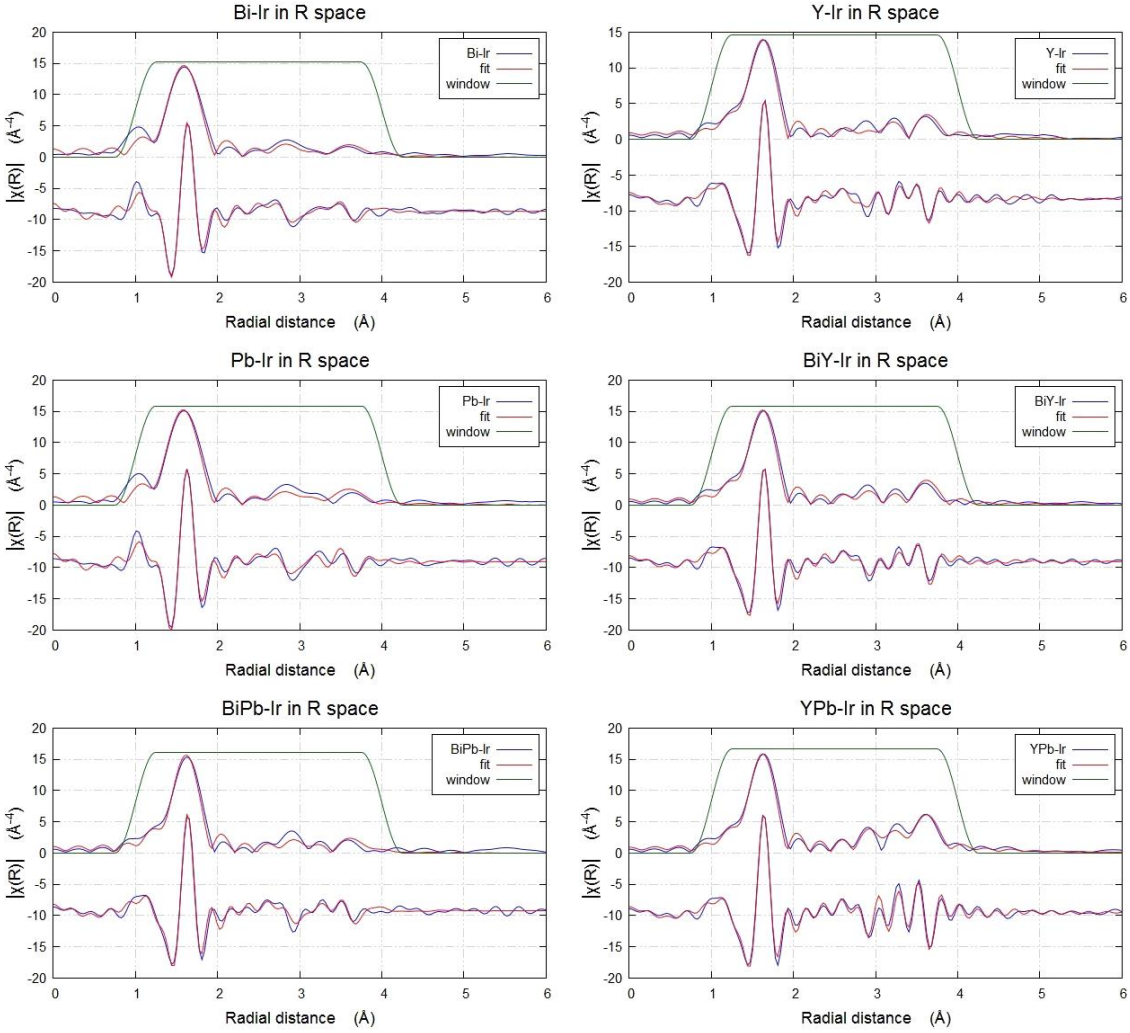

Figure S7. EXAFS fits of the pyrochlore catalysts in *R*-space shown using *k* weight 3.

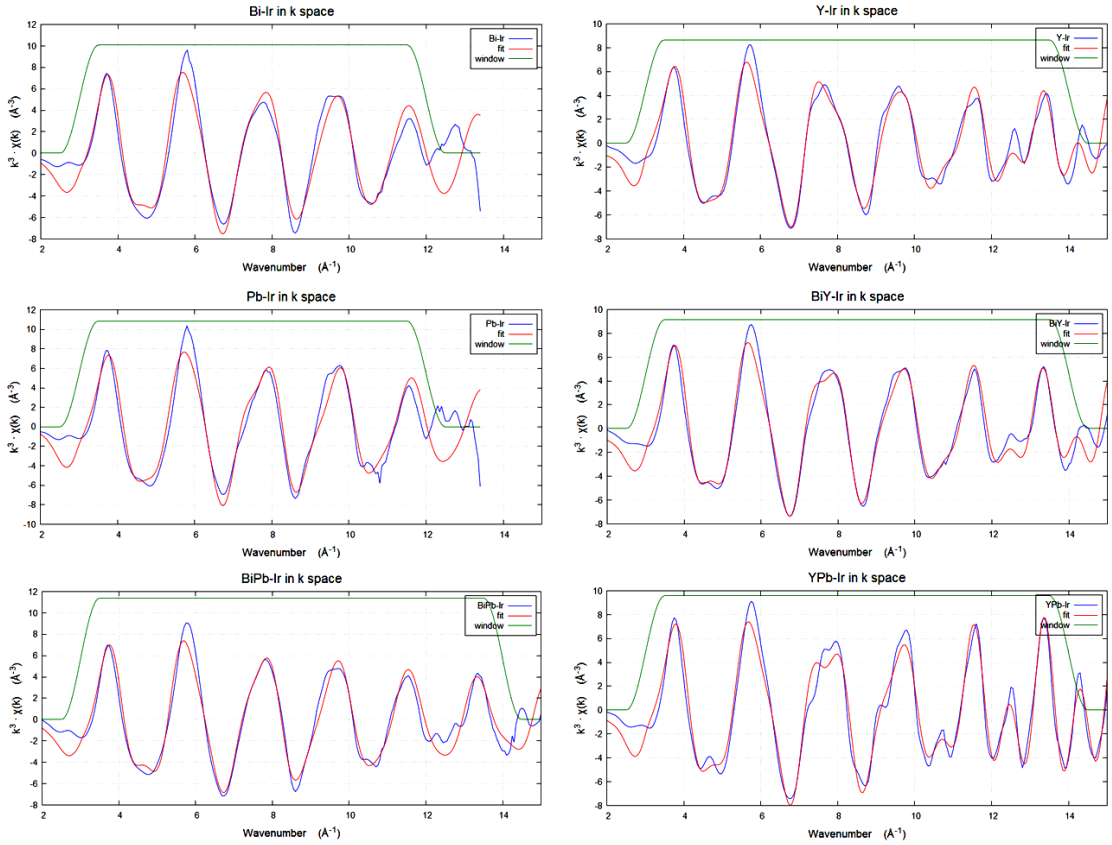

Figure S8. EXAFS fits of the pyrochlore catalysts in *k*-space shown using *k* weight 3.

Table S2. Details of the EXAFS fits of the pyrochlore catalysts.

Bi-Ir pyrochlore, 17 independent points, 7 variables, R value = 0.020							
Scattering path	N	S_0^2	σ^2, Å^2	ΔE_0, eV	*delr*	R_{eff}, Å	*R*, Å
O1.1	6	0.84(7)	0.002(1)	8.9(8)	-0.017(3)	2.0069	1.973(5)
O1.1 O1.1	12	0.84(7)	0.002(1)	8.9(8)	-0.017(3)	3.3345	3.28(1)
O1.1 O1.1	12	0.84(7)	0.002(1)	8.9(8)	-0.017(3)	3.5119	3.45(1)
Ir1.1	6	0.84(7)	0.01(1)	8.9(8)	-0.017(3)	3.6459	3.59(1)
Bi1.1	6	0.84(7)	0.02(1)	8.9(8)	-0.017(3)	3.6459	3.59(1)
O1.1 Ir1.1	12	0.84(7)	0.01(1)	8.9(8)	-0.017(3)	3.8298	3.77(1)
O1.2	6	0.84(7)	0.01(1)	8.9(8)	-0.017(3)	3.8732	3.81(1)
O1.1 O1.1	6	0.84(7)	0.01(1)	8.9(8)	-0.017(3)	4.0138	3.95(1)
O1.1 O1.1	6	0.84(7)	0.01(1)	8.9(8)	-0.017(3)	4.0138	3.95(1)

Y-Ir pyrochlore 21 independent points, 7 variables, R value = 0.023							
Scattering path	N	S_0^2	σ^2, Å^2	ΔE_0, eV	*delr*	R_{eff}, Å	*R*, Å
O1.1	6	0.80(5)	0.003(1)	9.1(8)	0.001(3)	1.9838	1.985(5)
O1.1 O1.1	12	0.80(5)	0.003(1)	9.1(8)	0.001(3)	3.2784	3.28(1)
O1.1 O1.1	12	0.80(5)	0.003(1)	9.1(8)	0.001(3)	3.4871	3.49(1)
Ir1.1	6	0.80(5)	0.007(1)	9.1(8)	0.001(3)	3.5729	3.57(1)
Y1.1	6	0.80(5)	0.011(2)	9.1(8)	0.001(3)	3.5729	3.57(1)
O1.1 Ir1.1	12	0.80(5)	0.01(2)	9.1(8)	0.001(3)	3.7703	3.77(1)
O1.2	6	0.80(5)	0.01(2)	9.1(8)	0.001(3)	3.8311	3.83(1)
O1.1 O1.1	6	0.80(5)	0.01(2)	9.1(8)	0.001(3)	3.9677	3.97(1)
O1.1 O1.1	6	0.80(5)	0.01(2)	9.1(8)	0.001(3)	3.9677	3.97(1)

Pb-Ir pyrochlore, 17 independent points, 6 variables, R value = 0.031							
Scattering path	N	S_0^2	σ^2, Å^2	ΔE_0, eV	*delr*	R_{eff}, Å	*R*, Å
O1.1	6	0.87(8)	0.003(1)	9(1)	-0.027(4)	2.0203	1.966(8)
O1.1 O1.1	12	0.87(8)	0.003(1)	9(1)	-0.027(4)	3.3568	3.27(1)
O1.1 O1.1	12	0.87(8)	0.003(1)	9(1)	-0.027(4)	3.5354	3.44(1)
Pb1.1	6	0.87(8)	0.01(1)	9(1)	-0.027(4)	3.6702	3.57(1)
Ir1.1	6	0.87(8)	0.02(2)	9(1)	-0.027(4)	3.6702	3.57(1)
O1.1 Ir1.1	12	0.87(8)	0.02(2)	9(1)	-0.027(4)	3.8554	3.75(2)
O1.2	6	0.87(8)	0.02(2)	9(1)	-0.027(4)	3.8991	3.79(2)
O1.1 O1.1	6	0.87(8)	0.02(2)	9(1)	-0.027(4)	4.0407	3.93(2)
O1.1 O1.1	6	0.87(8)	0.02(2)	9(1)	-0.027(4)	4.0407	3.93(2)

BiY-Ir pyrochlore, 21 independent points, 7 variables, R value = 0.021							
Scattering path	N	S_0^2	σ^2, Å^2	ΔE_0, eV	*delr*	R_{eff}, Å	*R*, Å
O1.1	6	0.79(5)	0.003(1)	9.7(7)	-0.013(3)	2.0069	1.981(5)
O1.1 O1.1	12	0.79(5)	0.003(1)	9.7(7)	-0.013(3)	3.3345	3.29(1)
O1.1 O1.1	12	0.79(5)	0.003(1)	9.7(7)	-0.013(3)	3.5119	3.47(1)
Bi1.1	3	0.79(5)	0.009(3)	9.7(7)	-0.013(3)	3.6459	3.60(1)
Y 1.1	3	0.79(5)	0.009(3)	9.7(7)	-0.013(3)	3.646	3.60(1)
Ir1.1	6	0.79(5)	0.007(2)	9.7(7)	-0.013(3)	3.6459	3.60(1)
O1.1 Ir1.1	12	0.79(5)	0.001(4)	9.7(7)	-0.013(3)	3.8298	3.78(1)
O1.2	6	0.79(5)	0.001(4)	9.7(7)	-0.013(3)	3.8732	3.82(1)
O1.1 O1.1	6	0.79(5)	0.001(4)	9.7(7)	-0.013(3)	4.0138	3.96(1)
O1.1 O1.1	6	0.79(5)	0.001(4)	9.7(7)	-0.013(3)	4.0138	3.96(1)

BiPb-Ir pyrochlore, 21 independent points, 7 variables, R value = 0.025							
Scattering path	N	S_0^2	σ^2, Å^2	ΔE_0, eV	*delr*	R_{eff}, Å	*R*, Å
O1.1	6	0.76(5)	0.002(1)	9.6(7)	-0.016(3)	2.0069	1.974(5)
O1.1 O1.1	12	0.76(5)	0.002(1)	9.6(7)	-0.016(3)	3.3345	3.28(1)
O1.1 O1.1	12	0.76(5)	0.002(1)	9.6(7)	-0.016(3)	3.5119	3.45(1)
Bi1.1	6	0.76(5)	0.010(3)	9.6(7)	-0.016(3)	3.6459	3.59(1)
Ir1.1	6	0.76(5)	0.03(3)	9.6(7)	-0.016(3)	3.6459	3.59(1)
O1.1 Ir1.1	12	0.76(5)	0.003(6)	9.6(7)	-0.016(3)	3.8298	3.77(1)
O1.2	6	0.76(5)	0.003(6)	9.6(7)	-0.016(3)	3.8732	3.81(1)
O1.1 O1.1	6	0.76(5)	0.003(6)	9.6(7)	-0.016(3)	4.0138	3.95(1)
O1.1 O1.1	6	0.76(5)	0.003(6)	9.6(7)	-0.016(3)	4.0138	3.95(1)

YPb-Ir pyrochlore, 21 independent points, 6 variables, R value = 0.035							
Scattering path	N	S_0^2	σ^2, Å^2	ΔE_0, eV	*delr*	R_{eff}, Å	*R*, Å
O1.1	6	0.80(6)	0.003(1)	9.7(8)	-0.021(3)	2.0203	1.977(6)
O1.1 O1.1	12	0.80(6)	0.003(1)	9.7(8)	-0.021(3)	3.3568	3.29(1)
O1.1 O1.1	12	0.80(6)	0.003(1)	9.7(8)	-0.021(3)	3.5354	3.46(1)
Ir1.1	6	0.80(6)	0.006(1)	9.7(8)	-0.021(3)	3.6702	3.59(1)
Pb1.1	3	0.80(6)	0.005(1)	9.7(8)	-0.021(3)	3.6702	3.59(1)
Y 1.1	3	0.80(6)	0.005(1)	9.7(8)	-0.021(3)	3.67	3.59(1)
O1.1 Ir1.1	12	0.80(6)	0.005(1)	9.7(8)	-0.021(3)	3.8554	3.77(1)
O1.2	6	0.80(6)	0.005(1)	9.7(8)	-0.021(3)	3.8991	3.82(1)
O1.1 O1.1	6	0.80(6)	0.005(1)	9.7(8)	-0.021(3)	4.0407	3.95(1)
O1.1 O1.1	6	0.80(6)	0.005(1)	9.7(8)	-0.021(3)	4.0407	3.95(1)

X–ray photoelectron spectroscopy

The binding energies of the acquired spectra were referenced to the C 1s line at 284.6 eV. Background subtraction has been performed according to Shirley[8] and the atomic sensitivity factors (ASF) of Scofield were applied to estimate the atomic composition.[9] The composition of Bi–Ir, Pb–Ir, BiPb–Ir, Y–Ir, and YPb–Ir were calculated based on integration of the Ir 4f, Bi 4f, Pb 4f and Y 3d spectra. Composition of BiY–Ir was determined from integration of Ir 4p3/2, Y 3s and Bi 4d5/2 due to the peak overlaps.

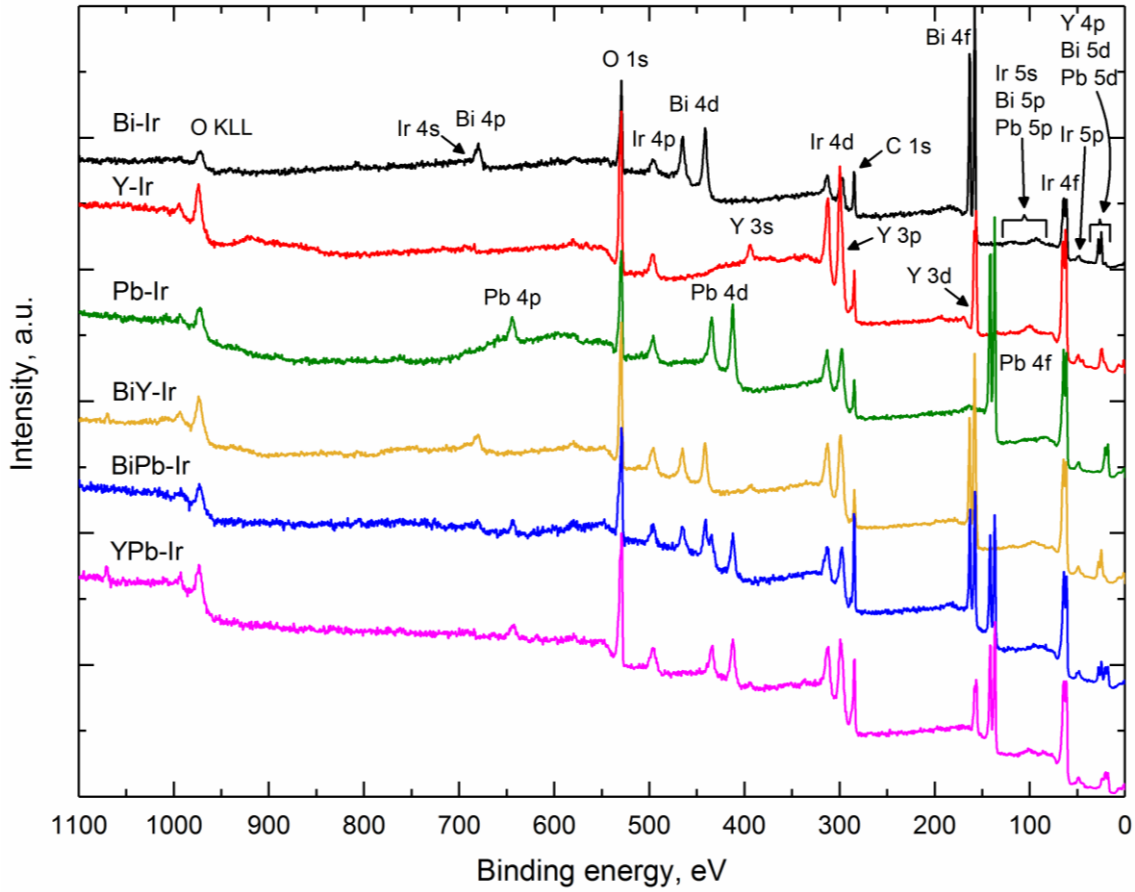

Figure S9. Survey XPS spectra of the pyrochlore materials.

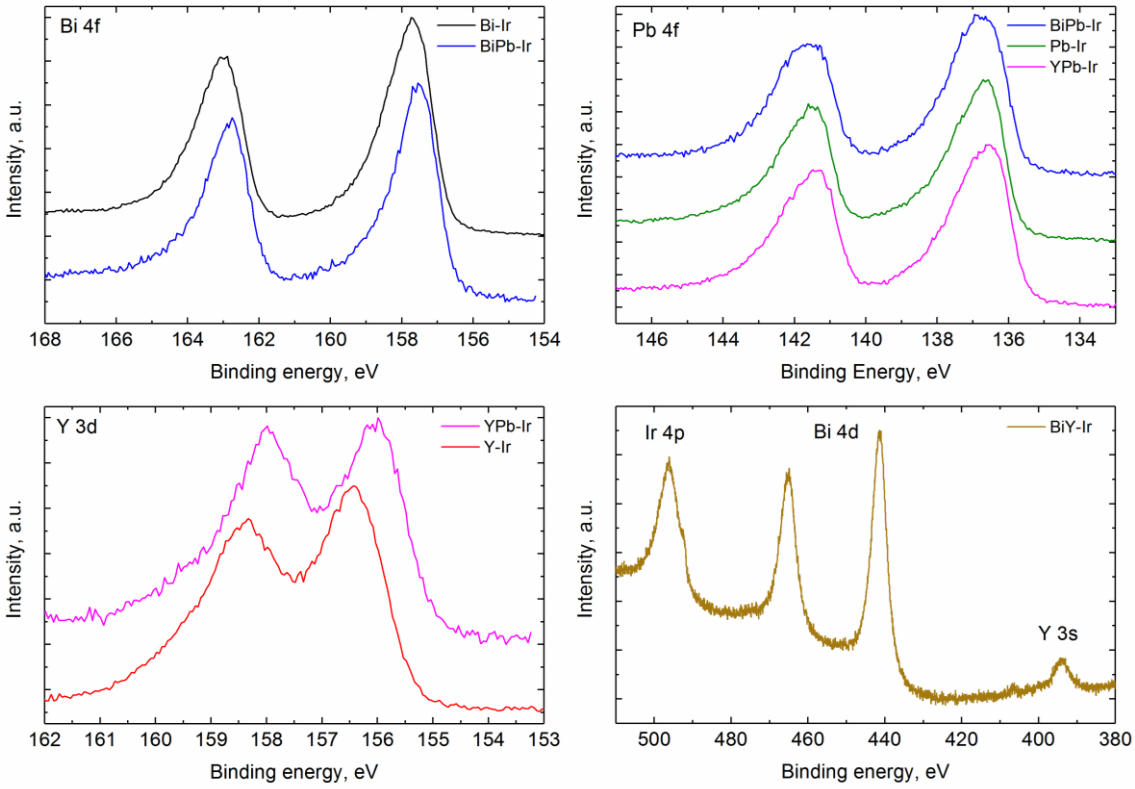

Figure S10. Normalized XPS spectra of the pyrochlore materials showing regions of *A* elements.

Electrochemical data

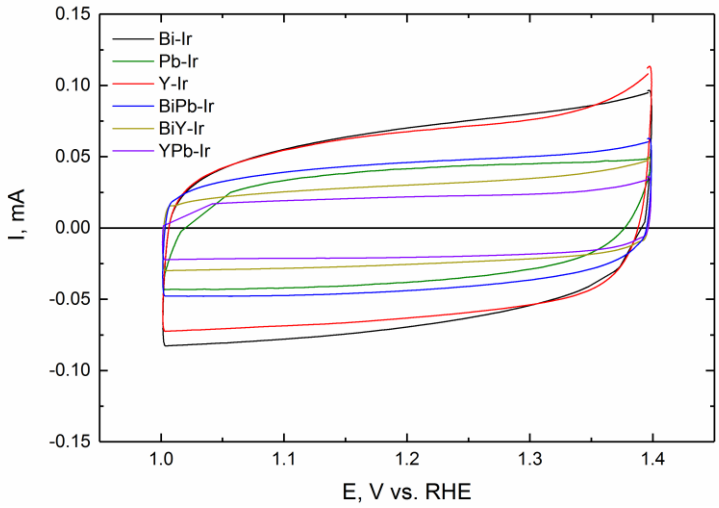

Figure S11. The 5th CV cycle of the pyrochlore catalysts used for surface charge determination (data is given in Table 2).

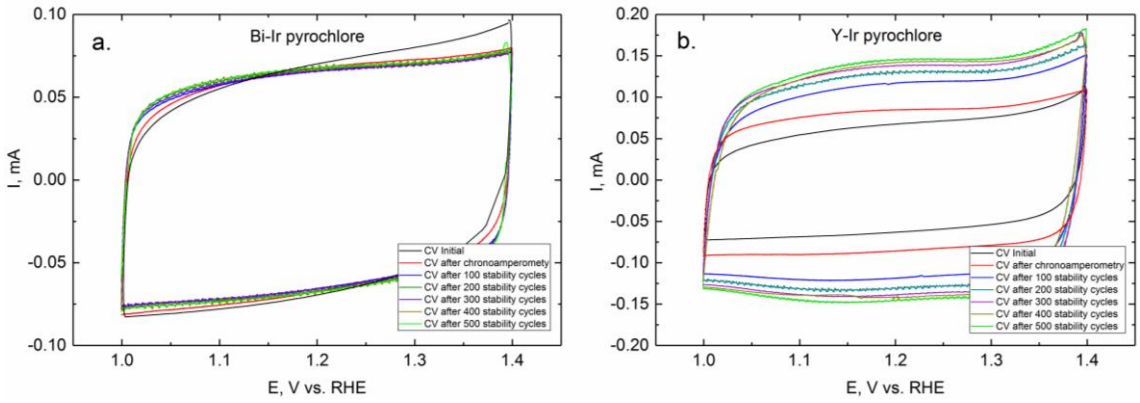

Figure S12. CVs of the Bi–Ir (a) and Y–Ir (b) samples taken before and during the stability measurements (every 100 cycles).

Density Functional Theory Calculations

All the structures (pyrochlores and other phases from the Materials Project database)[10] have been fully optimized using PBEsol as exchange-correlation functional in the Generalized Gradient Approximation[11] and the pseudopotentials from the Standard Solid State Pseudopotential library (SSSP accuracy)[12-13] as implemented in the Quantum ESPRESSO package.[14] The phase diagram module present in the Atomic Simulation Environment (ASE) has been used to generate the phase and Pourbaix diagrams.[15] The AiiDA package has been used to submit, retrieve and analyze the results of the simulations.[16]

In the phase stability diagram (Figure S10), the convex hull defines the stability frontier at 0K and was obtained by comparing the total energies of the pyrochlore with sum of the energies of the competing phases into which the pyrochlore structure can decompose. The stable compounds are indicated in the diagrams as green dots, while the unstable materials as red squares. We used Pourbaix diagrams (Figure S11) to address the issue of materials stability in water as a function of pH and electrochemical potential. The scheme used to produce these diagrams has been recently explained[17-18] and used to identify novel materials for light harvesting in a water splitting device and to study the stability of strontium ruthenate perovskite as a catalyst for the oxygen evolution reaction.[19-20]

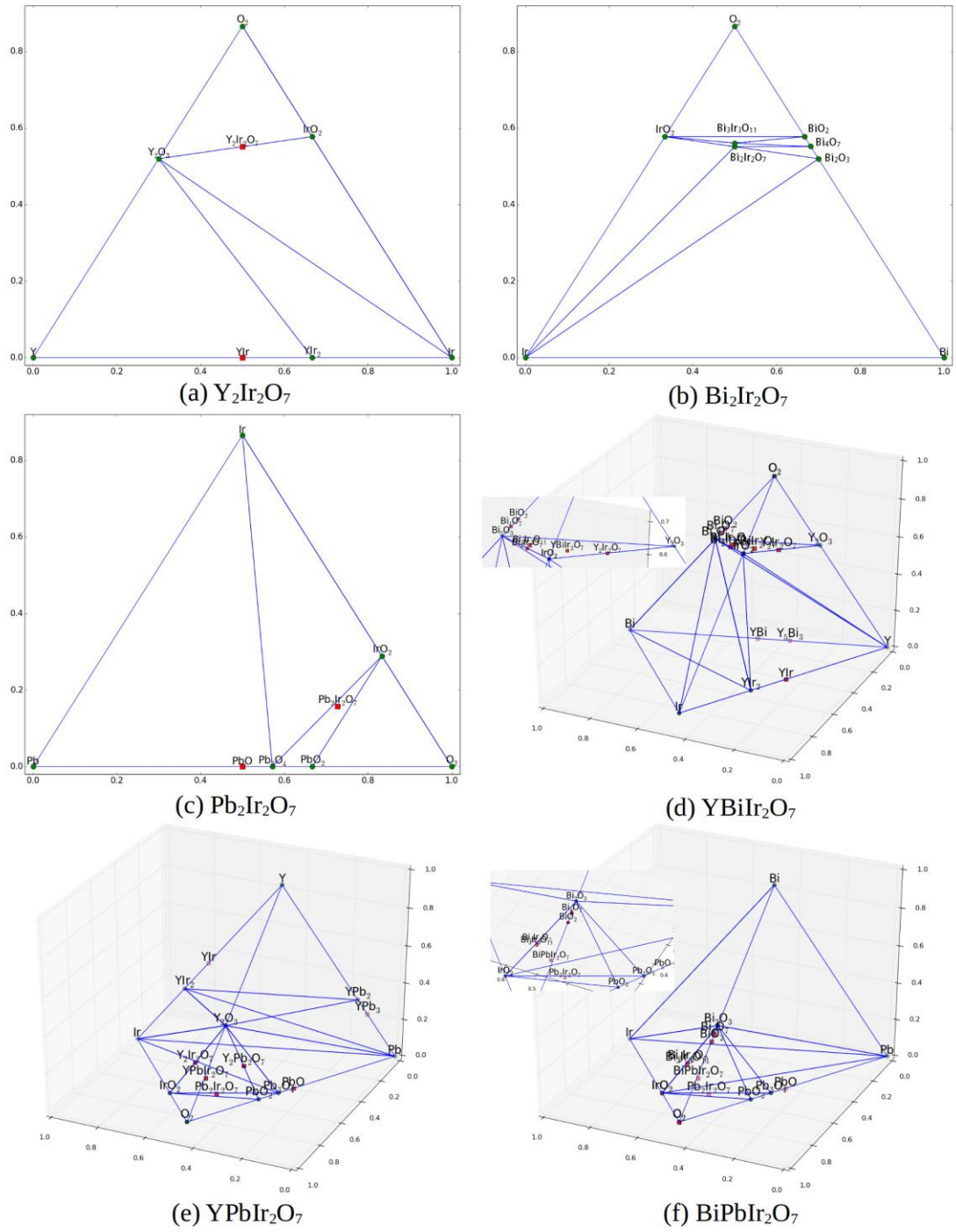

Figure S13. Calculated phase diagrams of the pyrochlore materials.

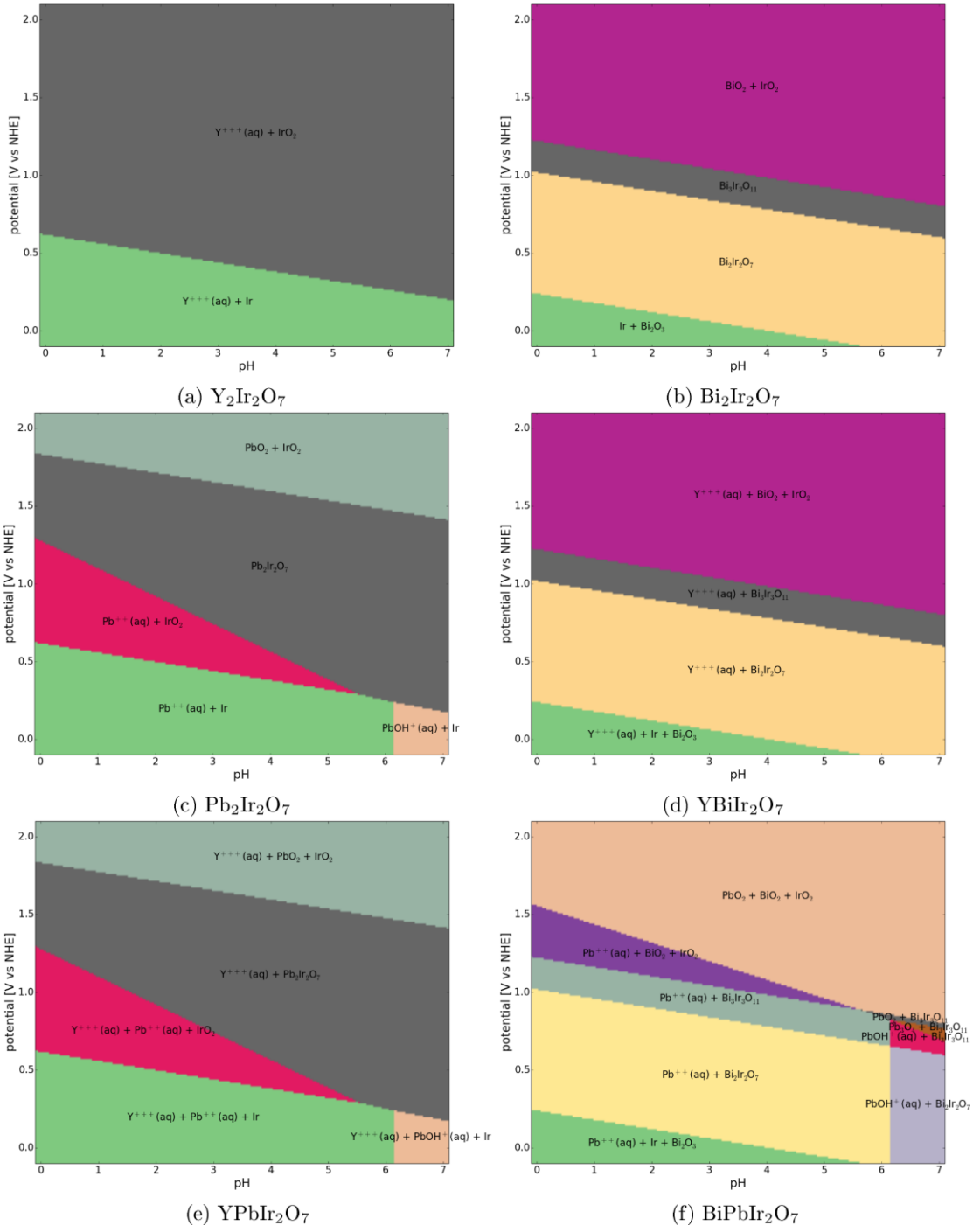

(a) $Y_2Ir_2O_7$ (b) $Bi_2Ir_2O_7$

(c) $Pb_2Ir_2O_7$ (d) $YBiIr_2O_7$

(e) $YPbIr_2O_7$ (f) $BiPbIr_2O_7$

Figure S14. Calculated Pourbaix diagrams of the pyrochlore materials.

References:

1. Abbott, D. F.; Lebedev, D.; Waltar, K.; Povia, M.; Nachtegaal, M.; Fabbri, E.; Copéret, C.; Schmidt, T. J., Iridium Oxide for the Oxygen Evolution Reaction: Correlation between Particle Size, Morphology, and the Surface Hydroxo Layer from Operando XAS. *Chem. Mater.* **2016,** *28*, 6591-6604.

2. Kieffer, J.; Karkoulis, D., PyFAI, a versatile library for azimuthal regrouping. *J. Phys.: Conf. Ser.* **2013,** *425*, 202012.

3. Rodríguez-Carvajal, J., Recent advances in magnetic structure determination by neutron powder diffraction. *Phys. B* **1993,** *192*, 55-69.

4. Juhás, P.; Davis, T.; Farrow, C. L.; Billinge, S. J. L., PDFgetX3: a rapid and highly automatable program for processing powder diffraction data into total scattering pair distribution functions. *J. Appl. Crystallogr.* **2013,** *46*, 560-566.

5. Muller, O.; Nachtegaal, M.; Just, J.; Lutzenkirchen-Hecht, D.; Frahm, R., Quick-EXAFS setup at the SuperXAS beamline for in situ X-ray absorption spectroscopy with 10 ms time resolution. *J. Synchrotron. Radiat.* **2016,** *23*, 260-266.

6. Newville, M., IFEFFIT: interactive XAFS analysis and FEFF fitting. *J. Synchrotron. Radiat.* **2001,** *8*, 322-324.

7. Ravel, B.; Newville, M., ATHENA, ARTEMIS, HEPHAESTUS: data analysis for X-ray absorption spectroscopy using IFEFFIT. *J. Synchrotron. Radiat.* **2005,** *12*, 537-541.

8. Shirley, D. A., High-Resolution X-Ray Photoemission Spectrum of the Valence Bands of Gold. *Phys. Rev. B* **1972,** *5*, 4709-4714.

9. Scofield, J. H., Hartree-Slater subshell photoionization cross-sections at 1254 and 1487 eV. *J. Electr. Spectr. Rel. Phenom* **1976,** *8*, 129-137.

10. Jain, A.; Ong, S. P.; Hautier, G.; Chen, W.; Richards, W. D.; Dacek, S.; Cholia, S.; Gunter, D.; Skinner, D.; Ceder, G.; Persson, K. A., Commentary: The Materials Project: A materials genome approach to accelerating materials innovation. *APL Mater.* **2013,** *1*, 011002.

11. Perdew, J. P.; Ruzsinszky, A.; Csonka, G. I.; Vydrov, O. A.; Scuseria, G. E.; Constantin, L. A.; Zhou, X.; Burke, K., Restoring the density-gradient expansion for exchange in solids and surfaces. *Phys. Rev. Lett.* **2008,** *100*, 136406.

12. Standard Solid State Pseudopotentials (SSSP). http://materialscloud.org/sssp/

13. Lejaeghere, K.; Bihlmayer, G.; Bjorkman, T.; Blaha, P.; Blugel, S.; Blum, V.; Caliste, D.; Castelli, I. E.; Clark, S. J.; Dal Corso, A.; de Gironcoli, S.; Deutsch, T.; Dewhurst, J. K.; Di Marco, I.; Draxl, C.; Dulak, M.; Eriksson, O.; Flores-Livas, J. A.; Garrity, K. F.; Genovese, L.; Giannozzi, P.; Giantomassi, M.; Goedecker, S.; Gonze, X.; Granas, O.; Gross, E. K.; Gulans, A.; Gygi, F.; Hamann, D. R.; Hasnip, P. J.; Holzwarth, N. A.; Iusan, D.; Jochym, D. B.; Jollet, F.; Jones, D.; Kresse, G.; Koepernik, K.; Kucukbenli, E.; Kvashnin, Y. O.; Locht, I. L.; Lubeck, S.; Marsman, M.; Marzari, N.; Nitzsche, U.; Nordstrom, L.; Ozaki, T.; Paulatto, L.; Pickard, C. J.; Poelmans, W.; Probert, M. I.; Refson, K.; Richter, M.; Rignanese, G. M.; Saha, S.; Scheffler, M.; Schlipf, M.; Schwarz, K.; Sharma, S.; Tavazza, F.; Thunstrom, P.; Tkatchenko, A.; Torrent, M.; Vanderbilt, D.; van Setten, M. J.; Van Speybroeck, V.; Wills, J. M.; Yates, J. R.; Zhang, G. X.; Cottenier, S., Reproducibility in density functional theory calculations of solids. *Science* **2016,** *351*, aad3000.

14. Giannozzi, P.; Baroni, S.; Bonini, N.; Calandra, M.; Car, R.; Cavazzoni, C.; Ceresoli, D.; Chiarotti, G. L.; Cococcioni, M.; Dabo, I.; Dal Corso, A.; de Gironcoli, S.; Fabris, S.; Fratesi, G.; Gebauer, R.; Gerstmann, U.; Gougoussis, C.; Kokalj, A.; Lazzeri, M.; Martin-Samos, L.; Marzari, N.; Mauri, F.; Mazzarello, R.; Paolini, S.; Pasquarello, A.; Paulatto, L.;

Sbraccia, C.; Scandolo, S.; Sclauzero, G.; Seitsonen, A. P.; Smogunov, A.; Umari, P.; Wentzcovitch, R. M., QUANTUM ESPRESSO: a modular and open-source software project for quantum simulations of materials. *J. Phys. Condens. Matter* **2009,** *21*, 395502.

15. Larsen, A.; Mortensen, J.; Blomqvist, J.; Castelli, I.; Christensen, R.; Dulak, M.; Friis, J.; Groves, M.; Hammer, B.; Hargus, C.; Hermes, E.; Jennings, P.; Jensen, P.; Kermode, J.; Kitchin, J.; Kolsbjerg, E.; Kubal, J.; Kaasbjerg, K.; Lysgaard, S.; Maronsson, J.; Maxson, T.; Olsen, T.; Pastewka, L.; Peterson, A.; Rostgaard, C.; Schiotz, J.; Schutt, O.; Strange, M.; Thygesen, K.; Vegge, T.; Vilhelmsen, L.; Walter, M.; Zeng, Z.; Jacobsen, K. W., The Atomic Simulation Environment - A Python library for working with atoms. *J. Phys. Condens. Matter* **2017**, 10.1088/1361-648X/aa680e.

16. Pizzi, G.; Cepellotti, A.; Sabatini, R.; Marzari, N.; Kozinsky, B., AiiDA: automated interactive infrastructure and database for computational science. *Comput. Mater. Sci.* **2016,** *111*, 218-230.

17. Persson, K. A.; Waldwick, B.; Lazic, P.; Ceder, G., Prediction of solid-aqueous equilibria: Scheme to combine first-principles calculations of solids with experimental aqueous states. *Phys. Rev. B* **2012,** *85*, 235438.

18. Castelli, I. E.; Thygesen, K. S.; Jacobsen, K. W., Calculated Pourbaix Diagrams of Cubic Perovskites for Water Splitting: Stability Against Corrosion. *Top. Catal.* **2013,** *57*, 265-272.

19. Castelli, I. E.; Hüser, F.; Pandey, M.; Li, H.; Thygesen, K. S.; Seger, B.; Jain, A.; Persson, K. A.; Ceder, G.; Jacobsen, K. W., New Light-Harvesting Materials Using Accurate and Efficient Bandgap Calculations. *Adv. Energy Mater.* **2015,** *5*, 1400915.

20. Kim, B.-J.; Abbott, D. F.; Cheng, X.; Fabbri, E.; Nachtegaal, M.; Bozza, F.; Castelli, I. E.; Lebedev, D.; Schäublin, R.; Copéret, C.; Graule, T.; Marzari, N.; Schmidt, T. J., Unraveling Thermodynamics, Stability, and Oxygen Evolution Activity of Strontium Ruthenium Perovskite Oxide. *ACS Catal.* **2017,** *7*, 3245-3256.